Rupture process and energy budget of the 29 July 2008 M_w 5.4 Chino Hills, California, earthquake

Guangfu Shao,[1,2] Chen Ji,[1,2] and Egill Hauksson[3]

Received 12 September 2011; revised 1 June 2012; accepted 5 June 2012; published 26 July 2012.

[1] The source model of the 2008 M_w 5.4 Chino Hills, California, earthquake is constrained using near-field seismic body waves recorded by the California Integrated Seismic Network (CISN). Finite fault inversions are preformed for the two fault models based on the nodal planes derived from the CISN moment tensor solution. The northeast dipping plane (strike = 289°; dip = 62°), which has a similar strike as the nearby Whittier fault, is chosen as the causative fault because it fits the data significantly better. Our inversion result indicates that the majority of the Chino Hills earthquake rupture occurred in a compact area. In particular, 48% of the total seismic moment (1.6×10^{17} Nm) was released by the failure of a 1.8 km^2 asperity located east of the hypocenter in a short time window from 0.4 to 0.8 s after the rupture initiation. The average slip is approximately 0.5 m but the maximum slip is 1.8 m. The average rupture velocity is 1.9 km/s. The static stress drop calculated using the slip model is up to 80 MPa and the average stress drop changes from 19 to 38 MPa, depending on the average schemes. The weighted average slip velocity is 6.5 m/s for entire rupture and is 11 m/s for the east asperity. The inferred available energy and radiated energy are 8×10^{13} J and 2.5×10^{13} J, respectively. Radiation efficiency is then 0.31, which is moderately low compared with previous earthquakes but consistent with the inferred high average fracture energy density, ranging from 6.5 to 14.8 MJ/m^2.

Citation: Shao, G., C. Ji, and E. Hauksson (2012), Rupture process and energy budget of the 29 July 2008 M_w 5.4 Chino Hills, California, earthquake, *J. Geophys. Res.*, *117*, B07307, doi:10.1029/2011JB008856.

1. Introduction

[2] On 29 July 2008, a M_w 5.4 earthquake hit the Los Angeles metropolitan area. It was located at a depth of 14.6 km beneath the Chino Hills, a series of hills marking the eastern boundary of the Los Angeles basin (Figure 1) [*Hauksson et al.*, 2008]. This event was widely felt across Southern California and as far away as Las Vegas, Nevada. The observed peak velocity was up to 39 cm/s, though very little damage was reported [*Hauksson et al.*, 2008]. The main shock was followed by about 150 $M_L > 1.0$ aftershocks in the first week. The largest aftershock had a M_L magnitude of 3.8, occurring ten minutes after the main shock.

[3] The Chino Hills earthquake occurred as a result of the ongoing north–south compression of the Transverse Ranges and the compression and lateral block movements within the Los Angeles basin [*Hauksson*, 1994]. The preliminary seismological analyses summarized in *Hauksson et al.* [2008] revealed an oblique faulting (mixture of thrust and strike-slip motions) on a high-angle fault plane (Table 1), with an abnormal high stress drop (~30 MPa). However, the causative fault has not been identified. There was no surface rupture during this event. Furthermore, its hypocenter was located at a potential intersection region between two mapped faults: the strike-slip-dominated Whittier fault and the oblique-thrust Chino fault (Figure 1). One of the nodal planes derived from the CISN moment tensor solution (Table 1) has a strike of 289° (hereafter referred as Plane I), close to that of the Whittier fault. However, the deformation on this portion of the Whittier fault was dominated by strike-slip motion in the late Quaternary, seemingly inconsistent with the significant thrust component of this earthquake. The other nodal plane (hereafter referred as Plane II) has a strike of 46° and a dip of 50°· Although Plane II roughly follows the Yorba Linda trend, a southwest trend of small earthquakes extending across this region into the Los Angeles basin [e.g., *Hauksson*, 1990; *Hauksson et al.*, 2008], it cannot be reasonably related with any mapped fault. Finally, the unusual sparse aftershocks did not cluster around either of the aforementioned nodal planes but were subhorizontally distributed within a depth range from 13 to 16 km [*Hauksson et al.*, 2008].

[4] The Chino Hills earthquake was well recorded by hundreds of CISN broadband and strong motion stations. Here we attempt to investigate the rupture process by

[1]Department of Earth Science, University of California, Santa Barbara, California, USA.
[2]Earth Research Institute, University of California, Santa Barbara, California, USA.
[3]Seismological Laboratory, Division of Geological and Planetary Sciences, California Institute of Technology, Pasadena, California, USA.

Corresponding author: G. Shao, Department of Earth Science, University of California, Santa Barbara, CA 93106, USA. (shao@umail.ucsb.edu)

0148-0227/12/2011JB008856

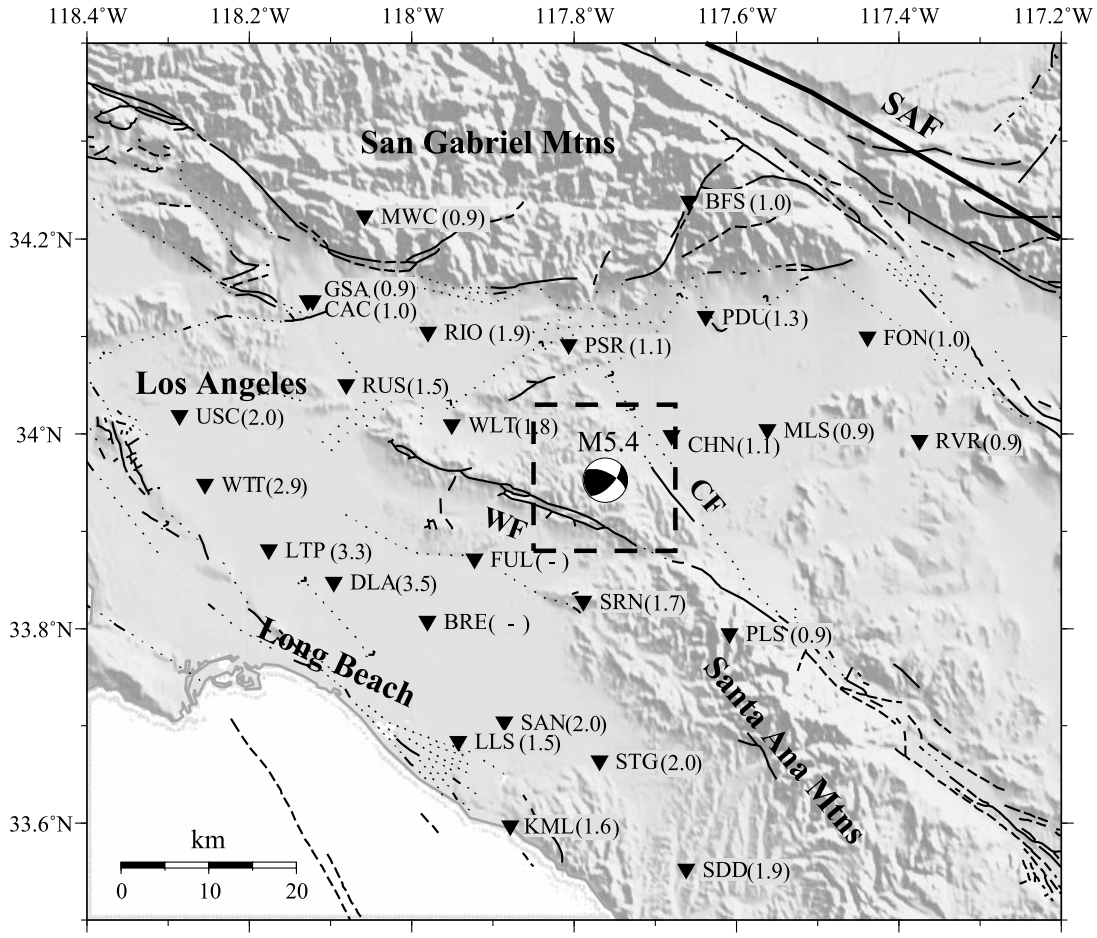

Figure 1. Focal mechanism and location map of the 2008 M_w 5.4 Chino Hills earthquake. Inverted triangles represent 26 selected seismic stations with station names on the right. Numbers inside parentheses indicate the *P* wave AAFs derived from 3-D to 1-D synthetics comparison (Figure 4). Dashed box marks the study area that is plotted in Figure 6. The solid, dashed, and dotted lines indicate the major fault traces in this area [*Jennings*, 1994]. SAF, San Andreas fault; WF, Whittier fault; CF, Chino fault. Note that we did not get the *P* wave AAFs for stations FUL and BRE because their 3-D synthetic *P* waves are significantly different from their 1-D synthetics.

analyzing the body waves recorded at these near-field stations. Owing to the proximity of the station distribution, we are able to determine the causative fault and retrieve the details of its heterogeneous rupture based on finite fault inversions [e.g., *Mori and Hartzell*, 1990]. This result has improved our understanding of the pattern of faulting and seismic hazards under the eastern Los Angeles basin.

2. Data and Finite Fault Inversions

[5] We analyzed the strong motion records of the 2008 Chino Hills earthquake downloaded from Southern California Data Center (SCDC). Only stations with epicentral distances less than 50 km were selected to avoid Moho reflections at greater distances. After correcting for instrument responses, we selected 20 *P* and 18 *SH* waves from 26 stations (Figure 1) by considering the signal-to-noise ratio of records and their azimuthal coverage. Both the *P* and *SH* waves include contributions from the near field and intermediate field waves. These waveforms were band-pass filtered from 0.16 to 2.5 Hz, integrated twice into displacement, and resampled at a time interval of 0.025 s. We windowed 2 s for *P* waves and 8 s for *SH* waves starting at their first *P* wave arrivals. We aligned the data and synthetics of *P* waves by their first arrivals. Since *P* wave first arrivals can

Table 1. Point Source Parameters

Hypocenter			Seismic Moment ($\times 10^{17}$ Nm)	Plane I			Plane II		
Longitude	Latitude	Depth (km)		Strike	Dip	Rake	Strike	Dip	Rake
−117.756°	33.946°	14.6	1.53	289°	62°	133°	46°	50°	38°

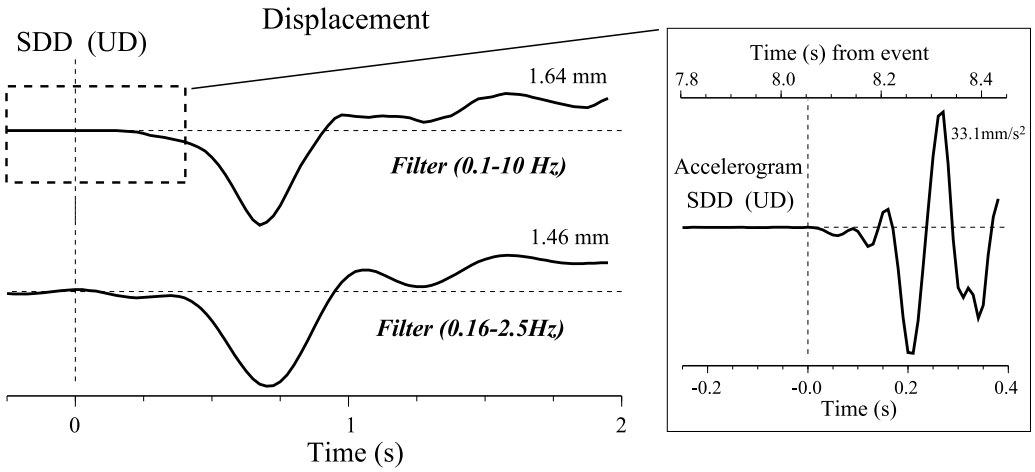

Figure 2. (left) Vertical component of the ground displacement recorded at station SDD. Number at the end of each trace shows its peak amplitude. The data are aligned by the picked *P* wave first arrivals. (right) The beginning 0.4 s of the recorded accelerogram with a sampling rate of 0.01 s. The horizontal axis on the top indicates the time aligned on the earthquake origin time. Vertical dashed line marks our picked first *P* wave arrival.

be clearly identified in the corresponding accelerograms as illustrated in Figure 2, the error of the alignment thus is less than 0.025 s, i.e., the resampling interval. However, the handpicked *SH* wave first arrivals are less precise, partially due to the weak initiation of the Chino Hills event discussed later (Figure 2). Therefore, we had first performed a preliminary inversion with *P* waves heavily weighted and *SH* waves down weighted, and then adjusted the SH picks slightly to achieve the best fits between the observed *SH* waveforms and synthetics of this preliminary inversion result. These timing values were not further adjusted.

[6] We calculate the synthetic earth response using the reflectivity method [*Zhu and Rivera*, 2002] and a 1-D layered velocity model (Figure 3a), averaged from the smoothed 1-D SoCal model [*Tan and Helmberger*, 2007]. We then correct for the 3-D basin structure effects using a semiempirical approach. *Tan and Helmberger* [2007] pointed out that the high-frequency *P* waveforms (0.5–2 Hz) recorded at LA basin could be modeled using 1-D Green's functions after adding path-dependent time shifts and multiplying by amplitude amplification factors (AAFs). They defined the AAFs as the amplitude ratios between records of a calibration event and the corresponding synthetics calculated with the smooth 1-D SoCal model. Their results show that AAFs are relatively stable and focal mechanism independent [*Tan and Helmberger*, 2007]. We

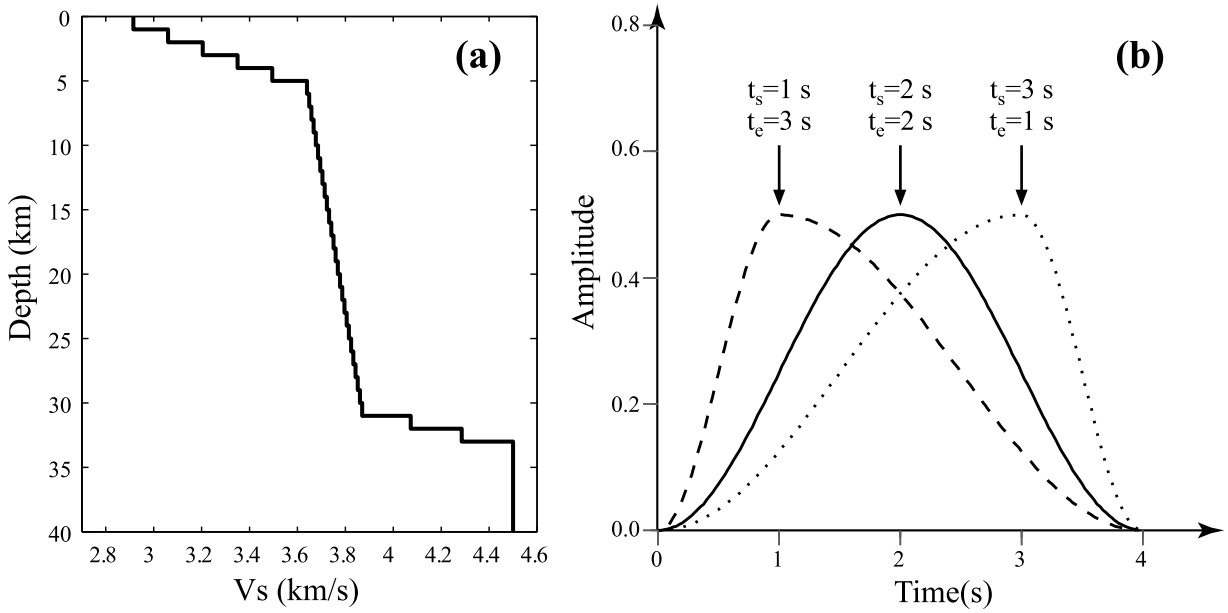

Figure 3. (a) The 1-D layered velocity model interpreted from the smoothed 1-D SoCal model [*Tan and Helmberger*, 2007]. (b) Three normalized asymmetric cosine functions with the same width but different starting and ending times [*Ji et al.*, 2003, Figure 3].

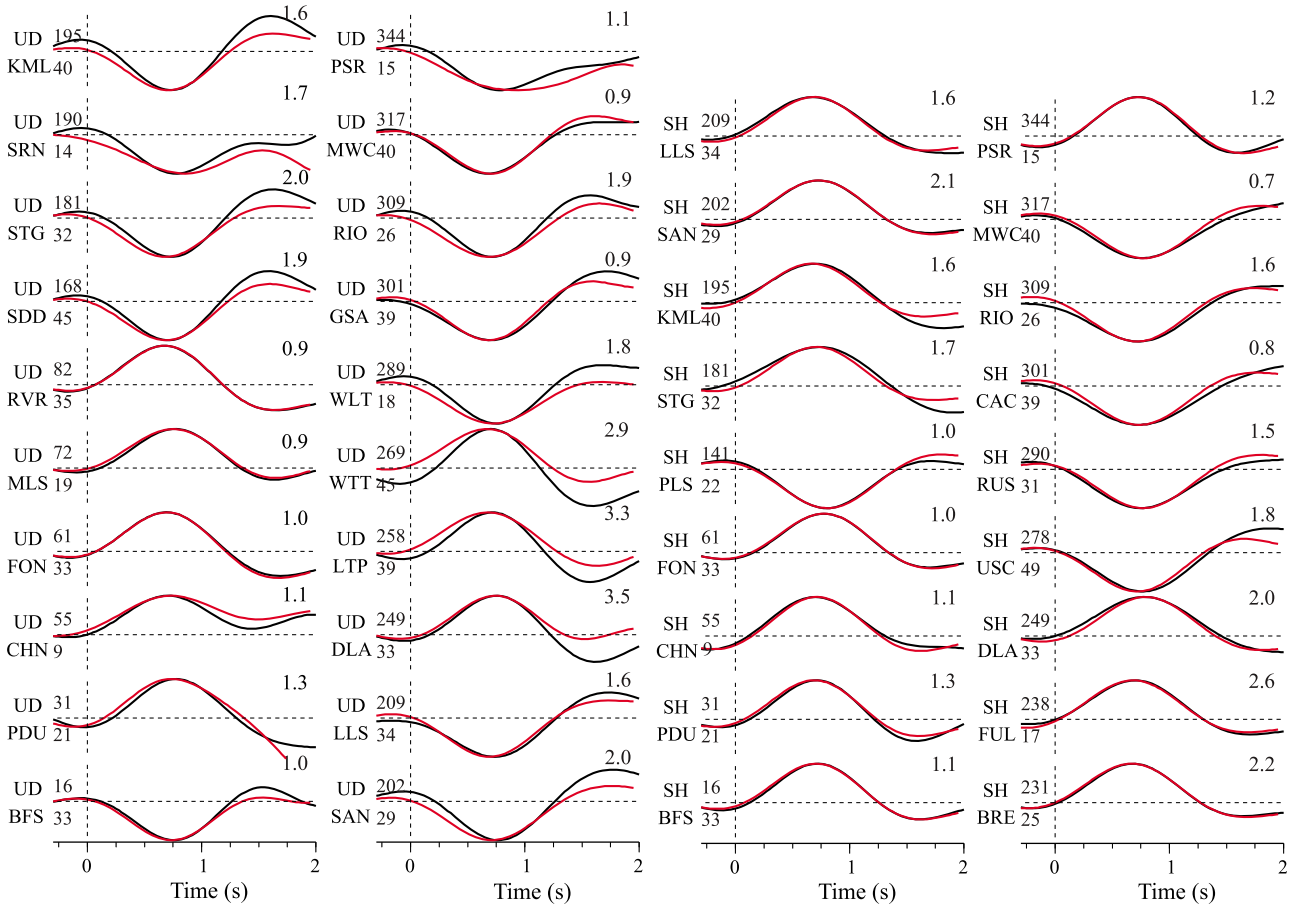

Figure 4. Comparison of synthetic waveforms generated based on the SCEC 3-D CVM-H model [*Süss and Shaw*, 2003] and the 1-D layered model (Figure 3a) using the same point source (Table 1). Both the 3-D (black lines) and 1-D (red lines) synthetics have been band-pass filtered between 0.16 and 1.0 Hz, aligned using a waveform cross-correlation procedure and normalized by their peak amplitudes. The number at the end of each trace indicates the amplitude ratio (3-D/1-D), which is adopted as the amplitude amplification factor (AAF) in inversions. Number above the beginning of each trace is the source azimuth in degrees and below is the epicentral distance in kilometers.

can correct the path-dependent time shifts by aligning the observations and synthetics with their first *P* wave arrivals. However, the amplitude discrepancies have to be considered. Due to the lack of a good calibration event, we estimate synthetic AAFs as the amplitude ratios between 3-D and 1-D synthetics calculated using the main shock moment tensor solution (Table 1). We adopt the Southern California Earthquake Center (SCEC) CVM-H model [*Hauksson*, 2000; *Süss and Shaw*, 2003] and the Spectral Element Method [*Komatitsch et al.*, 2004] to generate the 3-D synthetics, which are numerically accurate up to 1 Hz. We band-pass filtered these 1-D and 3-D synthetics from 0.16 Hz to 1.0 Hz before the estimating the AAFs. Figure 4 shows the comparison of filtered 1-D and 3-D synthetics, where the 1-D synthetics have been amplified by constant values, AAFs. The AAF corrections vary significantly. For instance, the values of *P* wave AAFs apparently correlate with the surface geology and change by a factor of 4 (from 0.9 to 3.5) among those stations (Figure 1). Though the AAF is likely frequency dependent, in this paper we simply assume that it is constant within the frequency region that we are interested in and leave more comprehensive analyses to a future effort. Since the predicted AAF corrections of *SH* waves are generally less precise than those of *P* waves because of the 3-D SCEC CVM-H model, we double weighted *P* waves relative to *SH* waves during the inversions.

[7] We construct the fault models based on the relocated CISN hypocenter and nodal planes I and II (Table 1) [*Hauksson et al.*, 2008], and name them as Model I and Model II, respectively. The fault plane size is 5.6 km (along strike) by 4.0 km (along dip) for the Model I and 4.4 km by 4.8 km for the Model II. In order to model the seismic signals up to 2.5 Hz, these fault planes are further discretized into 0.4 km by 0.4 km subfaults. The dimension of subfaults is assigned to be about one quarter of the shortest *S* wave wavelength used, which is generally proportional to the highest spatial resolution with the current data set [e.g., *Ihmlé and Ruegg*, 1997]. Totally, there are 140 subfaults for Model I and 132 subfaults for Model II. To take account the finiteness of individual subfaults, we further sampled each subfault with 9 uniformly distributed point sources [*Ji et al.*, 2002].

[8] Our finite fault inverse method carries out the waveform inversion in the wavelet domain and applies a

simulated annealing method [*Sen and Stoffa*, 1991] to simultaneously invert slip amplitude, rake angle, rupture initiation time, and slip rate function for each subfault [*Ji et al.*, 2002, 2003]. In this study, slip rate functions are approximated by asymmetric cosine functions with different starting and ending times (Figure 3b) [*Ji et al.*, 2003]. During the inversions, we let the slip amplitude vary from 0 to 2.5 m, and allowed the starting and ending times of the asymmetric slip rate function to change from 0.05 to 0.4 s. Thus, the value of risetime was limited between 0.1 and 0.8 s. The rake angle was limited from 115° to 160° for Model I and from 17° to 57° for Model II. Totally, there were 700 unknown parameters for Model I and 660 for Model II, as comparing with about 900 wavelet coefficients extracted from the seismic data. Because many of these wavelet coefficients are correlated, we further applied a derivative minimization smoothing constraint of fault slip to stabilize the inversions [*Ji et al.*, 2002]. An additional temporal constraint was also introduced to compress the roughness of rupture initiation time distribution [*Shao et al.*, 2011]. We represented the initiation time $t(x, y)$ at location (x, y) as the summation of a constant rupture field and a perturbation term $\delta t(x, y)$:

$$t(x,y) = \frac{L(x_o, y_o; x, y)}{\bar{v}} + \delta t(x,y), \quad (1)$$

where $L(x_o, y_o; x, y)$ is the on-fault distance from the hypocenter (x_o, y_o) and $\bar{v}$ is the rupture velocity averaged over the fault plane. If the perturbation field could be treated as white noise, we can smooth it by minimizing $\nabla^2(\delta t(x, y))$, similar to the approach used to smooth the fault slip. During this study, we used $\bar{v}$ as 2.0 km/s based on preliminary inversions without this temporal smoothing constraint, and allowed $\delta t(x, y)$ to vary between −1 s and 1 s.

3. Inversion Results

[9] We have performed multiple inversions for both fault geometries. Figure 6 compares the map views and vertical cross sections of the slip distributions of Model I (northeast dipping fault, Figures 6a and 6c) and Model II (southeast dipping fault, Figures 6b and 6d). We have also compared the synthetic seismograms of these two models with the observations in Figure 5. Model I explains the data significantly better than Model II, particularly for the *P* waves observed at stations located near *P* wave nodal lines (see Figure S2 in Text S1 in the auxiliary material), such as, SDD, DLA, LTP, WLT and GSA.[1] The variance reductions of the Model I are 70.4% for all the data and 74.7% for *P* waves only, which are 8.6% and 11.1% larger than those of the Model II (61.8% for all the data and 63.6% for *P* waves only). The largest discrepancies are observed at stations WLT and GSA, in which the synthetics of Model I match the data very well, but there are about 0.2 s offsets between the synthetics of Model II and observations. While the mismatch in amplitudes might be due to the inaccurate AAFs, these time shifts cannot be ignored because of the precise *P* wave alignments mentioned above. In the Model I, it should be noted that generally the fits to the *P* waves are better than the *SH* waves, which may due to the relatively less precise AAFs of *SH* waves.

[10] It is interesting to explore why the performances in waveform fitting between the two potential fault planes are so different. In map view, the high-slip regions of both models extend in N110°E to N290°E direction (Figures 6a and 6b), which is apparently a robust pattern required by the observations. To achieve such a spatial distribution, the source of the Model II must span a much larger depth range and locate shallower than that of the Model I, presumably due to the difference in the fault strike (Figures 6c and 6d). Our data set is composed of stations with epicenter distances as close as 9 km (CHN) and as far as 45 km (e.g., SDD), and includes both P and SH phases. These data are sensitive to the source depth relative to the hypocenter. In other words, changing the source depth would significantly affect the overall waveform fits. Although our study has used about 700 free parameters, the different waveform fits indicate that the discrepancies in the source depth distributions cannot be entirely compensated by only changing these variables. Therefore, the waveform data identify Model I as the preferred solution for the 2008 Chino Hills earthquake. The corresponding risetime and slip velocity distributions are shown in Figure 7. Snapshots of the slip on the fault plane in every 0.1 s are presented in Figure 8.

[11] Spatially, the slip distribution of the inferred solution is very compact (Figure 6c). The majority of oblique slip is limited to an approximately rectangular region of 3.2 km along strike and 1.2 km downdip (blue box, Figure 6c). The CISN hypocenter [*Hauksson et al.*, 2008] locates at the immediately up dip of this high-slip region. The total scalar seismic moment of the Chino Hills earthquake is 1.6×10^{17} Nm, consistent with the CISN moment tensor solution [*Hauksson et al.*, 2008]. The inverted peak slip is up to 1.8 m. If defining the "effective" fault area S_e [e.g., *Vassiliou and Kanamori*, 1982; *Venkataraman and Kanamori*, 2004] as the fault plane with more than 10% of the peak slip, it is 8.0 km^2. It has a simple average slip amplitude of 0.5 m and contributed 95% of the total seismic moment. Following *Mai et al.* [2005], we define the fault asperities as the fault patches with slip larger than one third of the peak slip, which results in two asperities for the Chino Hills earthquake. We refer them as east and west asperity respectively, according to their locations relative to the hypocenter (pink dashed boxes, Figure 6c). Those two asperities are corresponding to the two large peaks in the moment rate function addressed later (Figure 6, inset). The east asperity has an approximate dimension of 2.0 km (along strike) by 1.2 km (downdip). It contributes about one half of the total seismic moment and has a peak slip amplitude of about 1.8 m. The size and shape of the west asperity are, however, less well constrained. Its peak slip is about 0.7 m.

[12] Temporally, the rupture propagated in downdip direction after the initiation. As indicated by the moment rate function (Figure 6, inset), there was negligible slip during the first 0.4 s, before the explosive rupture of the east asperity. About 56% of the total seismic moment occurred between 0.4 and 0.8 s, producing 0.4–0.5 s wide pulses that dominate most P and SH records (Figure 5). The centroid time of the north asperity is 1 s after the rupture initiation. Because approximately 95% of the total seismic moment released from 0.4 to 1.6 s, the apparent source duration is 1.2 s for this event.

[1] Auxiliary materials are available in the HTML. doi:10.1029/2011JB008856.

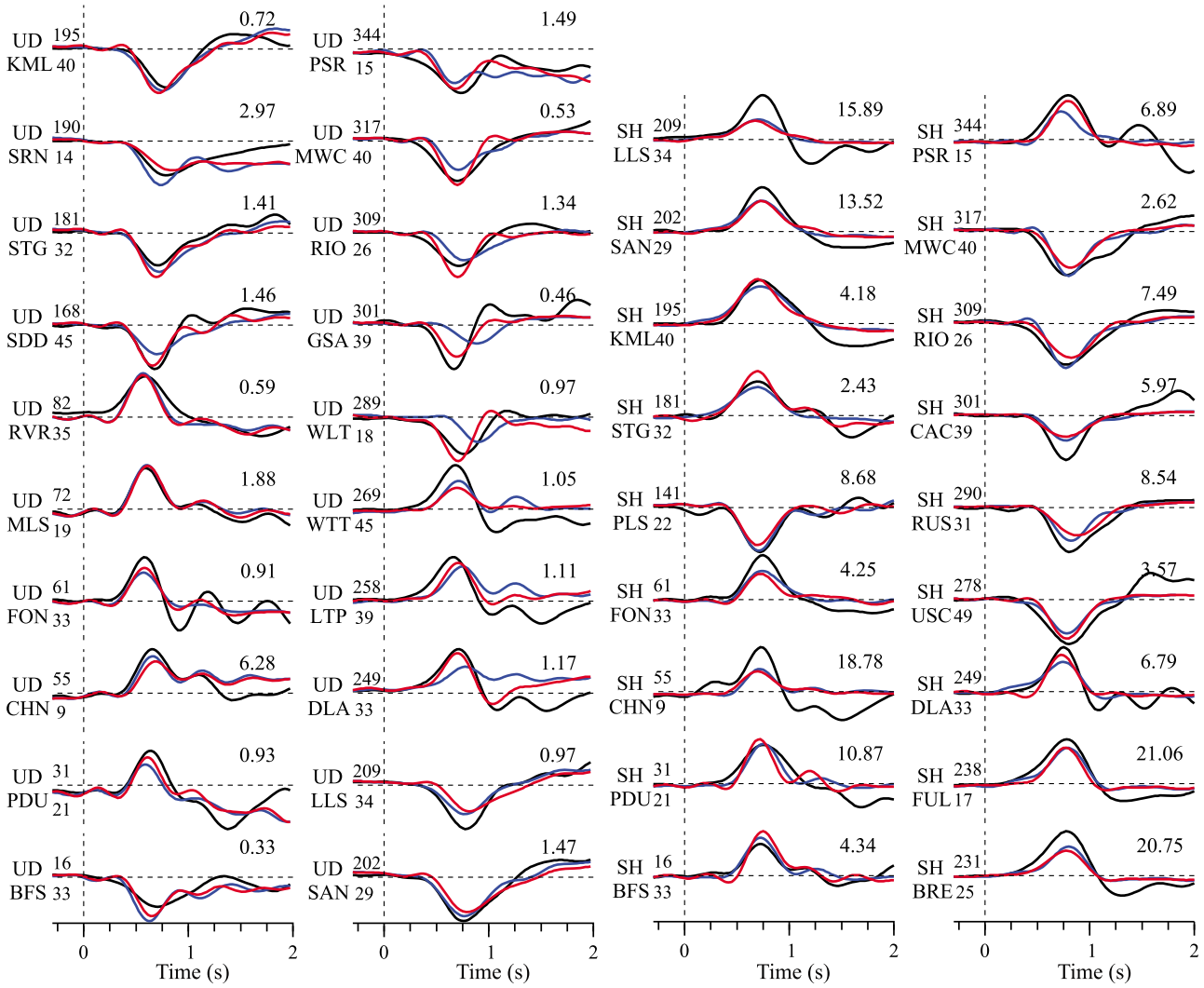

Figure 5. Comparison of observed waveforms (black lines) and synthetic seismograms calculated from Model I (red lines) and Model II (blue lines). All the waveforms have been band-pass filtered from 0.16 Hz to 2.5 Hz. The data and synthetics of *P* waves are aligned on their first *P* wave arrivals, where *SH* waves have been aligned with their synthetics of a preliminary model based on the waveform cross correlation. Both *P* and *SH* waves contain contributions from the near-field and intermediate waves. Number at the end of each trace shows the peak amplitude of observation in millimeters. Number above the beginning of each trace is the source azimuth in degrees and below is the epicentral distance in kilometers.

[13] The rupture velocity averaging from the hypocenter is about 1.9 km/s, but it locally increases to about 3.0 km/s over the high-slip region (Figures 6, 7, and 8). Although we allowed the risetime to change from 0.1 s to 0.8 s, the risetimes of the subfaults with large slip are very short, close to the allowed low bound limit (Figure 7a). Although there might be a relatively large uncertainty associated with the inverted risetime of individual subfaults, numerical tests indicated that the slip weighted average risetime over entire fault $\bar{T}_r$ (defined as $\bar{T}_r = \sum T_r^i D^i / \sum D^i$ where T_r^i, D^i are the risetime and slip of the ith subfault) is robust [*Ji et al.*, 2002]. Our calculation suggests that $\bar{T}_r$ is only 0.18 s. As pointed out by *Kanamori* [1994], the average slip velocity $\dot{D}$, defined as the ratio between the slip and risetime, is an important kinematic parameter and is proportional to the dynamic stress drop. Figure 7b shows the $\dot{D}$ estimation using our preferred slip model. It is up to 18 m/s and apparently has a positive correlation with fault slip. In fact, even the weighted average slip rate $\bar{\dot{D}}$, defined as $\sum D_i \dot{D}_i / \sum D_i$, is 6.5 m/s. It is noteworthy that the inversion based on Green's functions without the AAF corrections will result in a larger average slip velocity (7.4 m/s, Figure S3 in Text S1 in the auxiliary material).

[14] The weighted average slip velocity of the well-constrained east asperity is 11 m/s (Figure 7b). It is 9.8 m/s if we preform a simple average. Dependent on the slip partition, the particle velocity at one side of the fault would be around 4.9–5.5 m/s, larger than the highest surface ground velocity observed in a real earthquake (~4 m/s at station T076 during the 1999 Chi-Chi earthquake [e.g., *Ji et al.*, 2003]). However, such a large particle velocity is not dynamically implausible at a depth of 15 km. For instance, *Andrews*

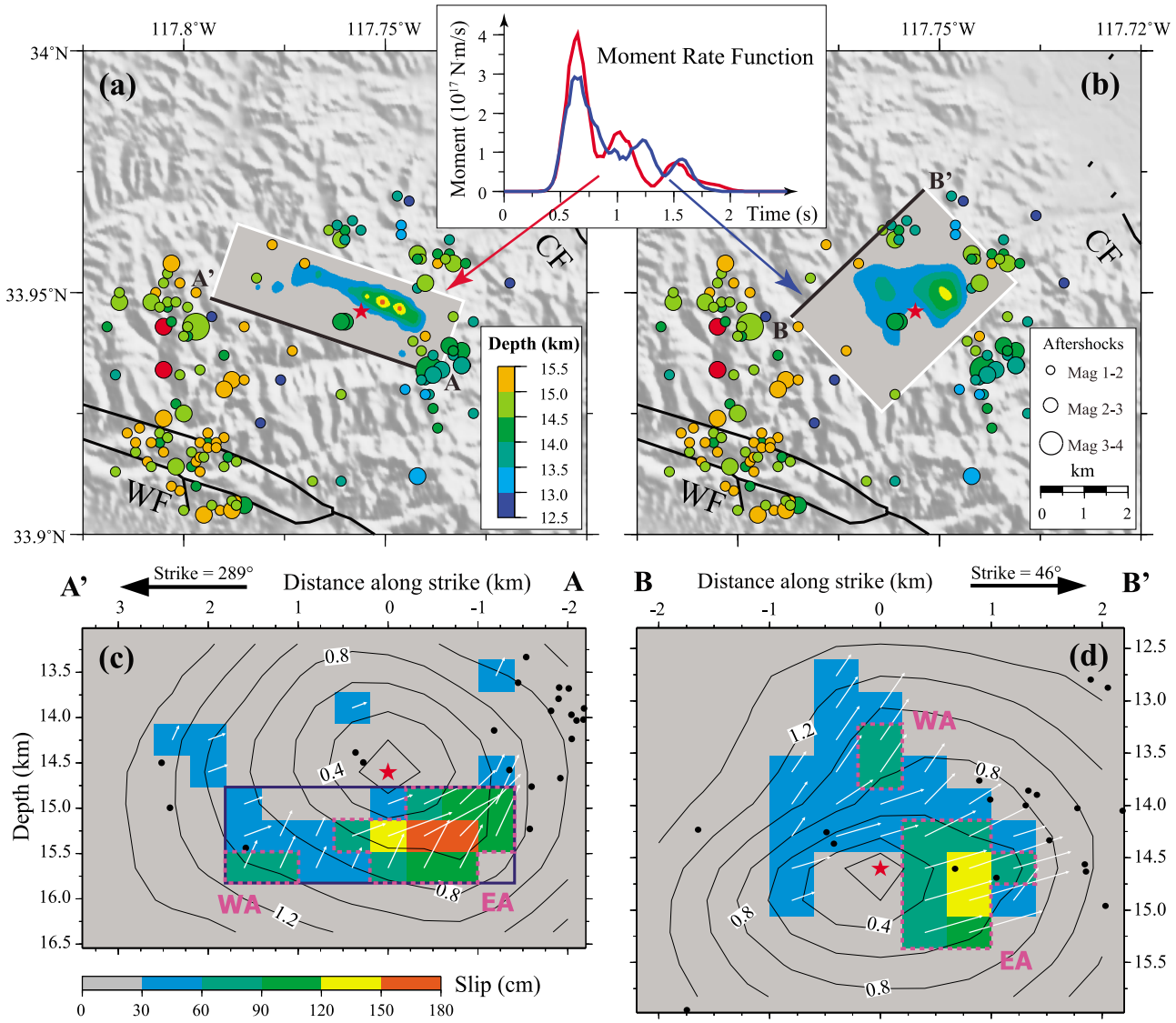

Figure 6. Comparison of inverted finite fault models on the two nodal planes. Inset compares the moment rate functions of Model I (red line) and Model II (blue line). (a) Surface projection of Model I (white box) superimposed on the shaded relief. Black line A-A′ indicates the top edge of the fault plane. Red star indicates the epicenter of the main shock. Filled circles show relocated aftershocks occurred in the first month [*Hauksson et al.*, 2008], with radiuses corresponding to their magnitudes and filled color denoting their depths. WF, Whittier fault; CF, Chino fault. (b) The same as Figure 6a but for Model II. (c) Cross section of the slip distribution of Model I. The vertical axis shows the absolute depth of the fault plane. Red star denotes its hypocenter. For each subfault, color denotes its dislocation amplitude and arrow indicates its motion direction of the hanging wall relative to the footwall. Black contours show rupture initiation time in seconds. Black dots denote the projections of the aftershocks located within 1 km from the fault plane. Blue box outlines the high-slip region and pink dashed boxes height the two major asperities. EA, east asperity; WA, west asperity. (d) The same as Figure 6c but for Model II.

[2004] suspected that the upper bound of particle velocity at a depth of 10 km is 10 m/s. It still raises concerns about whether our inferred slip velocity has been significantly overestimated. We shall note that a significantly overestimated slip velocity would imply that we have either significantly overestimated the fault slip or significantly underestimated the risetime. As we qualitatively discuss next, both of them are not plausible.

[15] As we have applied a slip smoothing constraint to stabilize the inversion, our solution shall be viewed as one of the smoother models if not the smoothest one among the solutions that could match the data. It is well known that the Laplace smoothing constraint tends to increase the inverted slip area of a target asperity, which results in an underestimated (rather than overestimated) the average slip. Furthermore, we have allowed the individual risetimes to change freely from 0.1 to 0.8 s, but the weighted average

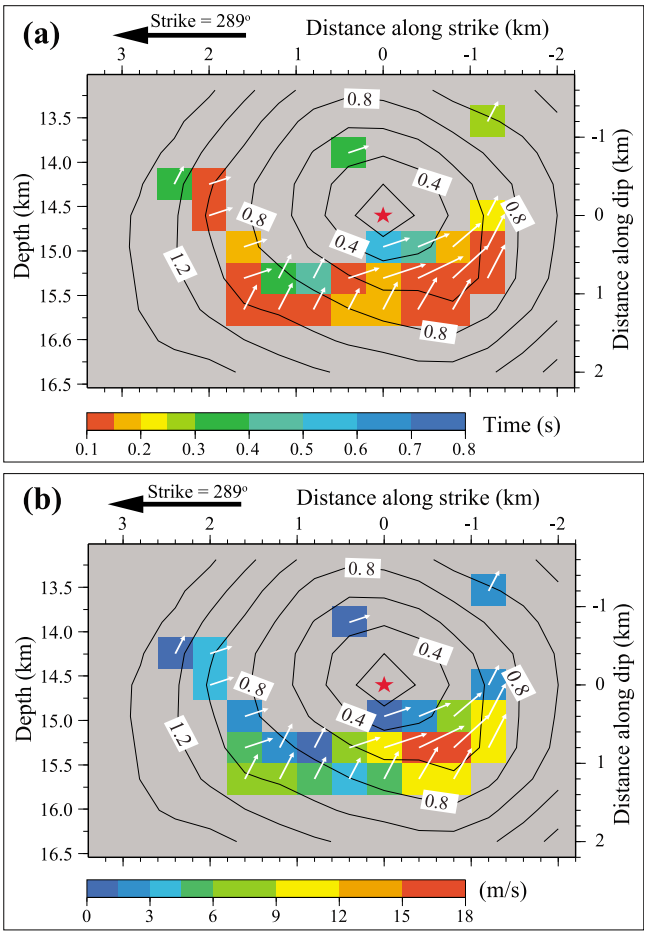

Figure 7. Distributions of (a) risetime and (b) slip velocity on the subfaults with slip amplitudes larger than 30 cm. Slip velocity is calculated as the ratio between slip amplitude and risetime. Red star indicates the hypocenter and white arrows show the motion directions on individual subfaults. Black contours denote the rupture initiation time in seconds.

risetime of the east asperity is only 0.13 s, nearly identical to the minimum risetime allowed. Note that if the data could not provide the constraint to the risetime, the inverted risetimes shall have a uniform distribution with an average value of 0.45 s. Hence, if the data cannot constrain the risetime precisely, the average value shall be larger. Here, our result might actually overestimate the risetime because we did not allow it to be shorter than 0.1 s.

[16] Most fault slip of the east asperity occurred from 0.4 to 0.8 s, corresponding to the 0.4 s wide sharp pulse in the moment rate function (Figure 6, inset). The average slip amplitude of this asperity is 1.24 m. Both the slip amplitude and duration of this pulse are well constrained by the *P* wave waveforms, such as the closest station CHN. Since the moment rate function is the spatial integration of the moment rate on the fault, in the first order we could approximate the duration of this pulse as the summation of the averaged risetime and the propagation time of rupture front across this asperity. Because the rupture propagation direction of this asperity, inferred from the shape of the rupture contours, is nearly normal to the slip directions (Figure 6c), it is reasonable to approximate the rupture front propagation as a mode III dynamic crack. The rupture velocity then cannot be faster than the shear wave speed (~3.7 km/s). So even the time for the rupture propagation equals to its upper limit, i.e., 0.4 s, the fault dimension would still be less than 1.5 km, which is just slightly larger than the current value (Figure 6c). Therefore, the average slip cannot be significantly reduced without violating such a fault dynamic constraint to the rupture velocity. This intuitive argument is confirmed by the results of an additional inversion test, which is preformed with a fixed maximum allowable slip amplitude of 0.8 m (see Figure S4 in Text S1 in the auxiliary material). Another potential scenario is to have a longer risetime. If the risetime is 0.3 s instead, the time left for rupture propagation would be reduced to only 0.1 s, suggesting a dimension of 0.4 km. Thus the inverted asperity shall be much more compact. As the seismic moment of this asperity is well constrained, we would expect a much higher average slip and then compensates the effect of longer risetime in producing a smaller slip velocity. However, as shown in Figure S5 in Text S1, this scenario is not plausible in terms of matching the data, because a compact source makes it difficult to explain observed differences among *P* wave waveforms at different stations (Figure 5).

[17] In short, our analyses suggest that the average slip velocity of the east asperity cannot be significantly smaller than our estimation of 11 m/s. However, we have to admit that the current data and our finite fault approach cannot constrain the upper bound of the average slip velocity. It is possible that the real average slip velocity is much higher. It is also noteworthy that the uncertainty of the slip velocity at individual subfaults shall be higher.

4. Discussions and Conclusions

4.1. Causative Fault of the 2008 Chino Hills Earthquake

[18] Considering the similarity of the strike of the Whittier fault and our preferred model (Model I), the Chino Hills earthquake could have ruptured a deep patch of the Whittier fault (Figure 9). Although the Whittier fault is dominant by strike-slip motion in the shallow depth, it cannot preclude the possibility of oblique thrust motion occurring on the deep part of the Whittier fault. If we define a fault plane using the Chino Hills hypocenter and the Whittier fault trace, the average dip angle would be around 75°, agreeing with the dip angle of the Whittier fault according to the 2002 U.S. National Seismic Hazard Maps. The averaged dip angle (75°) falls between the dip angle of this event (62°) and the mapped fault dip (>80°) in the shallow depth [*Bjorklund and Burke*, 2002]. Therefore, this hypothesis requires that the Whittier fault has a curved fault plane with fault dip gradually diminishing with depth (Figure 9), which in fact has been proposed in the previous studies [e.g., *Bjorklund and Burke*, 2002].

4.2. Static Stress Drop Associating With the Chino Hills Earthquake

[19] We calculate the on-fault static stress drop ($\Delta\vec{\sigma}_s$) from our preferred slip model (Figure 6c) using the software Coulomb 3.1 [*Lin and Stein*, 2004]. With a reasonable rigidity of 3.7×10^4 MPa inferred from the SoCal velocity

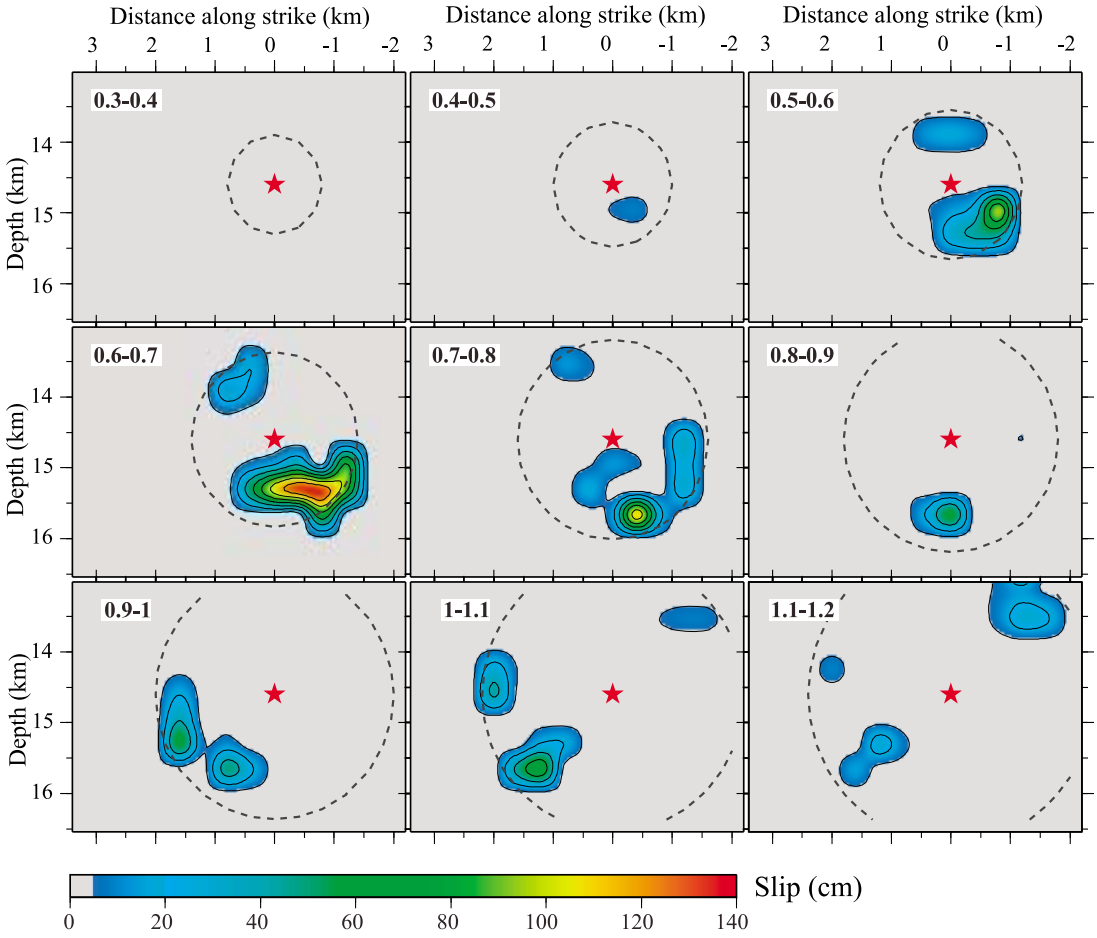

Figure 8. Snapshots of our preferred model from 0.3 s to 1.2 s. Numbers in the top left corner indicate the time window of each snapshot in seconds. Color denotes the slip amplitude. Red star shows the hypocenter location and dashed circle indicates a pseudorupture front at a reference velocity of 2 km/s.

model, the static stress drop is up to 80 MPa in the large slip region and varies significantly across the fault plane (Figure 10). The simple average static stress drop within the "effective" fault plane S_e defined above (the area with slip larger than 10% of the peak slip) is 22 MPa. Note that the estimation of average stress drop depends on the way to trim the slip model. The average stress drop is 19 MPa or 33 MPa if we use 5% or 20% of the peak slip as the trimming criteria. Nevertheless, the stress is significantly higher than the typical intraplate earthquakes [*Kanamori and Anderson*, 1975]. *Hauksson et al.* [2008] estimated the stress drop of this event based on an empirical relationship between the static stress drop and the rupture duration. Their estimation also yielded a large stress drop of 30 MPa.

[20] With spatial distributions of the fault slip and static stress drop, we can estimate the available elastic energy E_{T0} [*Kanamori and Rivera*, 2006] using the relation $E_{T0} = \frac{1}{2}\int_S \Delta\vec{\sigma}_s \cdot \vec{D}\, ds$, where vectors $\Delta\vec{\sigma}_s$ and $\vec{D}$ are static stress drops and dislocation amplitudes, respectively. Our calculation yields an available elastic energy of 8.0×10^{13} J. In many practices [e.g., *Venkataraman and Kanamori*, 2004], the available elastic energy is simply approximated as $\Delta\bar{\sigma}_s \bar{D} S_e/2$, where both the average static stress drop $\Delta\bar{\sigma}_s$ and the average slip $\bar{D}$ are estimated within an effective fault area S_e. If we define S_e as the area with slip larger than 10% of the peak slip, the estimated available energy using this approach is only 4.1×10^{13} J, half of the above estimation. Thus, ignoring the heterogeneous distributions of fault slip and stress drop, which are usually correlated, could lead to significant discrepancy in estimating available energy. This uncertainty shall be taken into consideration when we quantitatively address the available energy of an earthquake. One way to avoid this discrepancy is to adopt a weighted average approach to estimate the average static stress drop as we have done above for risetime and slip velocity, i.e., $\Delta\bar{\sigma} = \int_S \Delta\sigma_s D\, ds / \int_S D\, ds$. Note that $\int_S D\, ds$ is the seismic potency, which is often constrained well with seismic data. The weighted average stress drop is then equivalent to twice the ratio of the available energy to the total seismic potency. As the seismic potency is 4.2×10^6 m^3, the average stress drop is 38 MPa. Note that this approach also avoids the ambiguity in choosing the "effective" fault area, S_e mentioned above.

[21] Although it has been long recognized that the mean stress drop of moderate and large earthquake is about 3 MPa [e.g., *Kanamori and Anderson*, 1975], moderate earthquakes

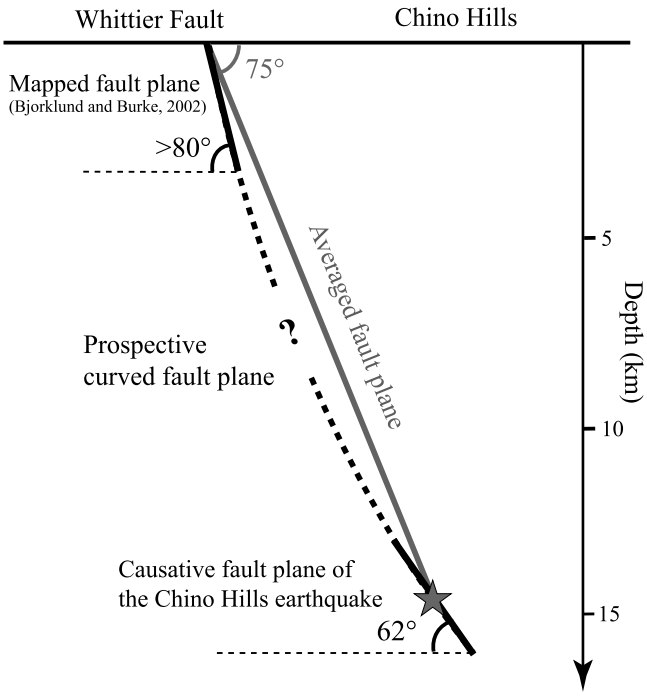

Figure 9. Schematic diagram of a prospective curved fault geometry of the Whittier fault. Star indicates the hypocenter of the 2008 Chino Hills earthquake.

with stress drops 1 or even 2 orders of magnitude larger are occasionally observed (see an early review in *Kanamori* [1994]). *Allmann and Shearer* [2009] recently estimated the stress drop of 2000 $m_b > 5.5$ earthquakes from 1990 to 2007. Although the median stress drop of their estimations is about 4 MPa, there are over ten M5.5–6 events with stress drop higher than 100 MPa. Some earthquakes with relatively normal average stress drops might also include subevents with abnormally high stress drops; i.e., what we find in the 2008 Chino Hills earthquake is not unique. For instance, the rupture of the 1984 M_w 6.2 Morgan Hill earthquake was found to include an isolated high-slip patch located at 14 km away from the hypocenter [*Beroza and Spudich*, 1988], which was associated with a static stress drop of 95 MPa according to a recent calculation [*Ripperger and Mai*, 2004]. Even though it had not been stated explicitly in the original literature, the failure of this high stress drop asperity was in a very high slip velocity. The inferred average slip velocity shall be over 10 m/s because the inverted slip is over 2 m and the risetime is 0.2 s [*Beroza and Spudich*, 1988]. To some extent, it is expectable that abnormally high slip velocity and abnormally high static stress drop accompany each other. Both of them are inferred from the similar observations, abnormal narrow displacement pulses in *P* or *SH* waves waveforms (also equivalent to abnormal high corner frequencies in *P* or *SH* wave displacement spectrum).

[22] While the dimension of the high stress drop asperities mentioned above is in the order of kilometers, a recent study

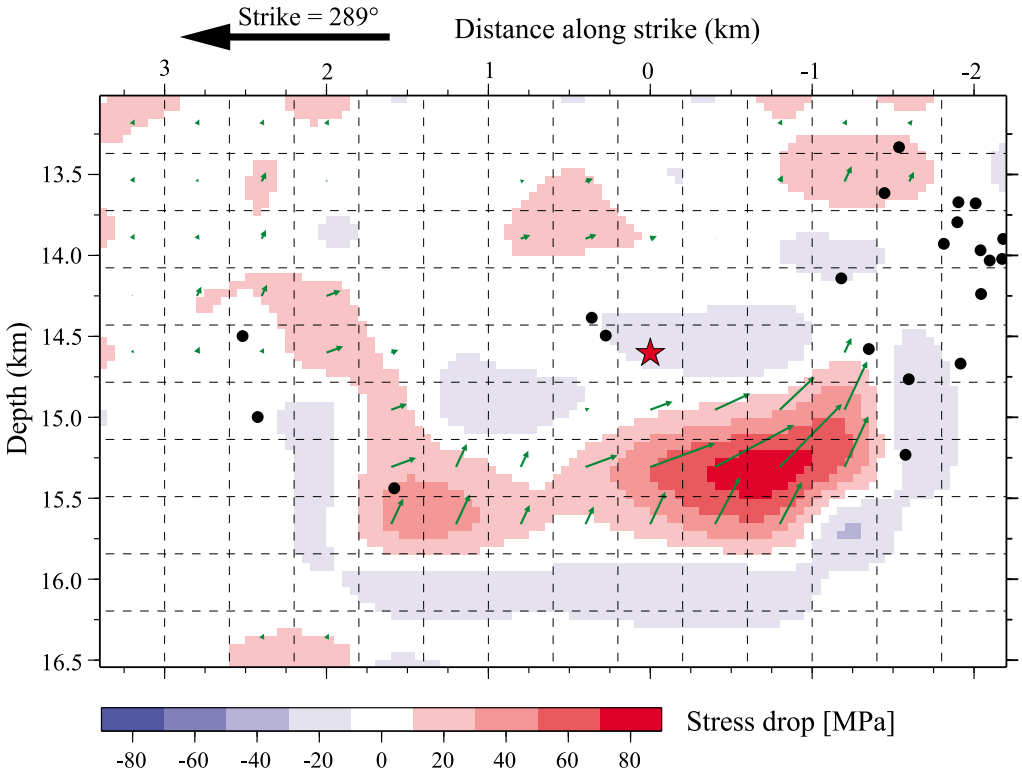

Figure 10. Interpolated static stress drop for the motion in the average rake angle direction (133°) calculated from our preferred model (Figure 6c) using the method of *Lin and Stein* [2004]. Green arrows show slip motion directions at individual subfaults. Black dots denote the projections of aftershocks located within 1 km from the fault plane.

suggested that such kinds of spatial stress heterogeneity could be in a dimension of tens of meters as well [*Dreger et al.*, 2007]. *Dreger et al.* [2007] found that several M_w 2.1 repeating earthquakes occurring on the San Andreas fault in Parkfield have normal average stress drops of 2.5–5.6 MPa but with large peak stress drops of 67–94 MPa. It is noteworthy that in this case the estimated peak stress drops are even higher than the maximum frictional fault strength at the depth of these ruptures. These interesting observations suggest that the fault zones could include strong patches that have a dimension from tens of meters to a few km and can sustain shear stress up to the order of 100 MPa. The failure of those asperities is associated with very high slip velocities, suggesting high dynamic stress drops [*Brune*, 1970]. However, the popularity and distribution of these strong fault patches in the crust fault system are not clear yet because to capture them requires close fault strong motion observations, which are still very limited.

4.3. Seismic-Radiated Energy and Fracture Energy

[23] We further calculate the radiated seismic energy E_s using the inverted moment rate function [*Vassiliou and Kanamori*, 1982] and yield a solution of 2.5×10^{13} J. The E_s/M_o ratio is then 1.6×10^{-4}, falling at the high end of the E_s/M_o ratios of previous $M_w > 4.5$ earthquakes (0.5×10^{-4} to 2×10^{-4}) [*Kanamori and Heaton*, 2000]. The apparent stress drop is then 5.9 MPa, considerably higher than the median value (1 MPa) [*Ide and Beroza*, 2001]. This relative large E_s/M_o ratio suggests that this earthquake has high seismic-radiated energy relative to its moment magnitude. This is consistent with the fact that this moderate event was felt as far away as Las Vegas, Nevada, about 350 km away. The large E_s/M_o ratio also suggests high dynamic stress drop [e.g., *Kanamori and Heaton*, 2000]. Because of the linear relationship between the dynamic stress drop and slip velocity [*Brune*, 1970], this macroscopic measurement is actually expected to be large. The radiation efficiency (defined as E_s/E_{T0}) [e.g., *Venkataraman and Kanamori*, 2004] is only 0.31, which is a moderately low value comparing to E_s/E_{T0} ratios of $M_w > 6.7$ earthquakes (0.25 to 1) [*Venkataraman and Kanamori*, 2004]. This relative small E_s/E_{T0} ratio indicates that most available energy is dissipated during the rupture process. A large E_s/M_o ratio and a moderately low radiation efficiency might seem inconsistent. But our result suggests that this could coexist if the earthquake also has a relatively large static stress drop.

[24] The total fracture energy of the Chino Hills earthquake might be approximated as the difference between the available energy and seismic-radiated energy [*Kanamori and Heaton*, 2000]. It is 5.2×10^{13} J in our study. If further assuming that the fracture energy was all used to break the "effective" fault plane defined above, the average fracture energy density G is 6.5 MJ/m^2.

[25] We can also directly estimate the average fracture energy density using the average kinematic parameters. *Rice et al.* [2005] derived the following scaling relation for a 2-D slip weakening pulse models:

$$G = \frac{\mu \bar{D}^2}{\pi L} F(v_r) g(R/L), \qquad (2)$$

where $\bar{D}$ is the average slip. $F(v_r)$ is a function of rupture velocity v_r and is $\sqrt{1 - v_r^2/\beta^2}$ for mode III rupture. $g(R/L)$ is a complex function of R/L, changing from 1 (for $R/L = 0$) to 2 (for $R/L = 1$). For completeness, following *Rice et al.* [2005], we have approximated the pulse length L as the product of rupture velocity and the average risetime, i.e., $v_r T_r$, and estimated the average fracture energy density G of this earthquake with this relation as well. We find that the estimates based on these two different approaches are consistent within the uncertainties of these methods. Using the average slip of 0.5 m, the average rupture velocity of 1.9 km/s and risetime of 0.18 s, equation (2) yields the range of the fracture energy density from 7.4 to 14.8 MJ/m^2, slightly larger than the above estimate of 6.5 MJ/m^2. The average fracture energy estimated for other earthquakes varies from 0.1 to 9 MJ/m^2 [*Rice et al.*, 2005]. Nevertheless, the fracture energy density is again relatively high. The high fracture energy might explain why this event could accumulate such large slip within this small fault patch.

4.4. Aftershocks and Slip Distribution

[26] In Figure 6a, we compare the relocated $M_L \geq 1$ aftershocks which occurred in the first month with the inverted slip distribution in a map view. Figure 6c compares the slip distribution with selected aftershocks located within 1 km from the preferred fault plane. Interestingly, such a high stress drop earthquake triggered very few aftershocks in the vicinity of its high-slip region (Figure 6c), inconsistent with the aftershock sequence of other high stress events in the Southern California, such as the 1987 Whittier Narrow, 1991 Sierra Madre, and 1994 Northridge earthquakes [*Hartzell and Iida*, 1990; *Shearer*, 1997; *Wald*, 1992; *Wald et al.*, 1996; *Zeng et al.*, 1993]. The aftershocks were subhorizontally distributed within a depth range from 13 to 16 km [*Hauksson et al.*, 2008]. The majority of main shock rupture occurred in a narrower depth range from 15 to 16 km, near the bottom of this subhorizontal aftershock zone (Figure 6). This may indicate that the major slip area of the main shock has released most accumulated stress and becomes a low-stress zone, and the stress concentration is shifted to the shallower part. Perhaps a detailed analysis of the Chino Hills aftershock sequence could help us to better understand this.

[27] **Acknowledgments.** We thank the constructive comments of the Associate Editor and three anonymous reviewers. We also thank Ross Stein and Martin Mai for their help on the stress drop calculation, Hiroo Kanamori for his help in radiated energy estimation, and Ralph Archuleta for the discussion of dynamic rupture. The strong motion waveforms were downloaded from the CISN data center (http://www.data.scec.org/). Most figures were created using the Generic Mapping Tools (GMT) software [*Wessel and Smith*, 1998]. This work is partially supported by Dol-USGS 08CRGR0001 and partially supported by the Southern California Earthquake Center (SCEC) 120044, which is funded by the National Science Foundation (NSF) Cooperative Agreement EAR-0106924 and the U.S. Geological Survey (USGS) Cooperative Agreement 02HQAG0008. This article is contribution 1262 of SCEC and 0965 of the Institute for Crustal Studies (ICS).

References

Allmann, B. P., and P. M. Shearer (2009), Global variations of stress drop for moderate to large earthquakes, *J. Geophys. Res.*, *114*, B01310, doi:10.1029/2008JB005821.

Andrews, D. J. (2004), Rupture models with dynamically determined breakdown displacement, *Bull. Seismol. Soc. Am.*, *94*(3), 769–775, doi:10.1785/0120030142.

Beroza, G. C., and P. Spudich (1988), Linearized inversion for fault rupture behavior: Application to the 1984 Morgan Hill, California, earthquake, *J. Geophys. Res.*, *93*(B6), 6275–6296, doi:10.1029/JB093iB06p06275.

Bjorklund, T., and K. Burke (2002), Four-dimensional analysis of the inversion of a half-graben to form the Whittier fold-fault system of the Los Angeles basin, *J. Struct. Geol.*, *24*(9), 1369–1387, doi:10.1016/S0191-8141(01)00147-X.

Brune, J. N. (1970), Tectonic stress and the spectra of seismic shear waves from earthquakes, *J. Geophys. Res.*, *75*(26), 4997–5009, doi:10.1029/JB075i026p04997.

Dreger, D., R. M. Nadeau, and A. Chung (2007), Repeating earthquake finite source models: Strong asperities revealed on the San Andreas fault, *Geophys. Res. Lett.*, *34*, L23302, doi:10.1029/2007GL031353.

Hartzell, S., and M. Iida (1990), Source complexity of the 1987 Whittier Narrows, California, earthquake from the inversion of strong motion records, *J. Geophys. Res.*, *95*(B8), 12,475–12,485, doi:10.1029/JB095iB08p12475.

Hauksson, E. (1990), Earthquakes, faulting, and stress in the Los Angeles basin, *J. Geophys. Res.*, *95*(B10), 15,365–15,394, doi:10.1029/JB095iB10p15365.

Hauksson, E. (1994), The 1991 Sierra Madre earthquake sequence in Southern California: Seismological and tectonic analysis, *Bull. Seismol. Soc. Am.*, *84*(4), 1058–1074.

Hauksson, E. (2000), Crustal structure and seismicity distribution adjacent to the Pacific and North America plate boundary in Southern California, *J. Geophys. Res.*, *105*(B6), 13,875–13,903, doi:10.1029/2000JB900016.

Hauksson, E., K. Felzer, D. Given, M. Giveon, S. Hough, K. Hutton, H. Kanamori, V. Sevilgen, S. Wei, and A. Yong (2008), Preliminary report on the 29 July 2008 Mw 5.4 Chino Hills, eastern Los Angeles basin, California, earthquake sequence, *Seismol. Res. Lett.*, *79*(6), 855–866, doi:10.1785/gssrl.79.6.855.

Ide, S., and G. C. Beroza (2001), Does apparent stress vary with earthquake size?, *Geophys. Res. Lett.*, *28*(17), 3349–3352, doi:10.1029/2001GL013106.

Ihmlé, P. F., and J.-C. Ruegg (1997), Source tomography by simulated annealing using broad-band surface waves and geodetic data: Application to the *Mw* = 8.1 Chile 1995 event, *Geophys. J. Int.*, *131*(1), 146–158, doi:10.1111/j.1365-246X.1997.tb00601.x.

Jennings, C. W. (1994), Fault activity map of California and adjacent areas, with locations and ages of recent volcanic eruptions, *Geol. Data Map 6*, Div. of Mines and Geol., Calif. Dep. of Conserv., Sacramento.

Ji, C., D. J. Wald, and D. V. Helmberger (2002), Source description of the 1999 Hector Mine, California, earthquake, part I: Wavelet domain inversion theory and resolution analysis, *Bull. Seismol. Soc. Am.*, *92*(4), 1192–1207, doi:10.1785/0120000916.

Ji, C., D. V. Helmberger, D. J. Wald, and K.-F. Ma (2003), Slip history and dynamic implications of the 1999 Chi-Chi, Taiwan, earthquake, *J. Geophys. Res.*, *108*(B9), 2412, doi:10.1029/2002JB001764.

Kanamori, H. (1994), Mechanics of earthquakes, *Annu. Rev. Earth Planet. Sci.*, *22*, 207–237, doi:10.1146/annurev.ea.22.050194.001231.

Kanamori, H., and D. L. Anderson (1975), Amplitude of the Earth's free oscillations and long-period characteristics of earthquake source, *J. Geophys. Res.*, *80*(8), 1075–1078, doi:10.1029/JB080i008p01075.

Kanamori, H., and T. H. Heaton (2000), Microscopic and macroscopic physics of earthquakes, in *Geocomplexity and the Physics of Earthquakes*, *Geophys. Monogr. Ser.*, vol. 120, edited by J. B. Rundle, D. L. Turcotte, and W. Klein, pp. 147–163, AGU, Washington, D. C., doi:10.1029/GM120p0147.

Kanamori, H., and L. Rivera (2006), Energy partitioning during an earthquake, in *Earthquakes: Radiated Energy and the Physics of Faulting*, *Geophys. Monogr. Ser.*, vol. 170, edited by R. Abercrombie et al., pp. 3–13, AGU, Washington, D. C., doi:10.1029/170GM03.

Komatitsch, D., Q. Liu, J. Tromp, P. Süss, C. Stidham, and J. H. Shaw (2004), Simulations of ground motion in the Los Angeles basin based upon the spectral-element method, *Bull. Seismol. Soc. Am.*, *94*(1), 187–206, doi:10.1785/0120030077.

Lin, J., and R. S. Stein (2004), Stress triggering in thrust and subduction earthquakes and stress interaction between the southern San Andreas and nearby thrust and strike-slip faults, *J. Geophys. Res.*, *109*, B02303, doi:10.1029/2003JB002607.

Mai, P. M., P. Spudich, and J. Boatwright (2005), Hypocenter locations in finite-source rupture models, *Bull. Seismol. Soc. Am.*, *95*(3), 965–980, doi:10.1785/0120040111.

Mori, J., and S. Hartzell (1990), Source inversion of the 1988 Upland, California, earthquake: Determination of a fault plane for a small event, *Bull. Seismol. Soc. Am.*, *80*(3), 507–518.

Rice, J. R., C. G. Sammis, and R. Parsons (2005), Off-fault secondary failure induced by a dynamic slip pulse, *Bull. Seismol. Soc. Am.*, *95*(1), 109–134, doi:10.1785/0120030166.

Ripperger, J., and P. M. Mai (2004), Fast computation of static stress changes on 2D faults from final slip distributions, *Geophys. Res. Lett.*, *31*, L18610, doi:10.1029/2004GL020594.

Sen, M. K., and P. L. Stoffa (1991), Nonlinear one-dimensional seismic waveform inversion using simulated annealing, *Geophysics*, *56*(10), 1624–1638.

Shao, G., X. Li, C. Ji, and T. Maeda (2011), Focal mechanism and slip history of the 2011 M_w 9.1 off the Pacific coast of Tohoku earthquake, constrained with teleseismic body and surface waves, *Earth Planets Space*, *63*(7), 559–564, doi:10.5047/eps.2011.06.028.

Shearer, P. M. (1997), Improving local earthquake locations using the L1 norm and waveform cross correlation: Application to the Whittier Narrows, California, aftershock sequence, *J. Geophys. Res.*, *102*(B4), 8269–8283, doi:10.1029/96JB03228.

Süss, M. P., and J. H. Shaw (2003), P wave seismic velocity structure derived from sonic logs and industry reflection data in the Los Angeles basin, California, *J. Geophys. Res.*, *108*(B3), 2170, doi:10.1029/2001JB001628.

Tan, Y., and D. Helmberger (2007), A new method for determining small earthquake source parameters using short-period *P* waves, *Bull. Seismol. Soc. Am.*, *97*(4), 1176–1195, doi:10.1785/0120060251.

Vassiliou, M. S., and H. Kanamori (1982), The energy release in earthquakes, *Bull. Seismol. Soc. Am.*, *72*(2), 371–387.

Venkataraman, A., and H. Kanamori (2004), Observational constraints on the fracture energy of subduction zone earthquakes, *J. Geophys. Res.*, *109*, B05302, doi:10.1029/2003JB002549.

Wald, D. J. (1992), Strong motion and broadband teleseismic analysis of the 1991 Sierra Madre, California, earthquake, *J. Geophys. Res.*, *97*(B7), 11,033–11,046, doi:10.1029/92JB00565.

Wald, D. J., T. H. Heaton, and K. W. Hudnut (1996), The slip history of the 1994 Northridge, California, earthquake determined from strong ground motion, teleseismic, GPS, and leveling data, *Bull. Seismol. Soc. Am.*, *86*(1), S49–S70.

Wessel, P., and W. H. F. Smith (1998), New, improved version of Generic Mapping Tools released, *Eos Trans. AGU*, *79*(47), 579, doi:10.1029/98EO00426.

Zeng, Y., K. Aki, and T.-L. Teng (1993), Source inversion of the 1987 Whittier Narrows earthquake, California, using the isochron method, *Bull. Seismol. Soc. Am.*, *83*(2), 358–377.

Zhu, L., and L. A. Rivera (2002), A note on the dynamic and static displacements from a point source in multilayered media, *Geophys. J. Int.*, *148*(3), 619–627, doi:10.1046/j.1365-246X.2002.01610.x.